Bachelor Thesis:

Comparison of Mott-Hubbard-transition on the Bethe-lattice and the 2D-square-lattice

Supervisors:

Associate Prof. Dr. Alessandro Toschi
Dipl.-Ing. Patrick Chalupa

Institute of Solid State Physics
Quantum many body physics group
Technische Universität Wien

by

Mathias Pelz
1429137

Abstract

Many intriguing phenomena are encountered in studies of strongly correlated electron systems. One of the most prominent among them is arguably the Mott-Hubbard-metal-insulator-transition (MIT), a phase transition between a metal and an insulator, which is originated by the electronic interaction. The presence of strong correlations poses however specific problems to the forefront theoretical treatment. For instance a challenging aspect, that has been recently discovered is the existence of multiple divergences of the irreducible vertex functions, observed in several many-electron models. Among them also the Hubbard model, solved by means of the dynamical mean field theory (DMFT). For this case, depending on the lattice model studied, a peculiar discrepancy in the low-temperature behavior of the vertex divergences lines was found. To study, whether this discrepancy is rooted in the different behavior of the MIT, the coexistence regions for the Bethe- and the 2D-square-lattice are analysed in the thesis. This comparison shows also the influence of the shape of the density of states (DOS) on the MIT. For the numerical DMFT calculations the *w2dynamics* package has been used, which is an efficient implementation of a continuous-time quantum Monte Carlo impurity solver. For both lattices the self-energy and the double occupancy at different temperatures are calculated. From these quantities the critical interaction values U_{c1} and U_{c2} as a function of temperature are obtained.

Kurzfassung

Viele faszinierende Phänomene treten bei Untersuchungen von stark korrelierten Elektronensystemen auf. Einer der bekanntesten unter ihnen ist wohl der Mott-Hubbard-Metall-Isolator-Übergang (MIT), ein Phasenübergang zwischen einem Metall und einem Isolator, der durch die elektronische Wechselwirkung entsteht. Das Vorhandensein starker Korrelationen wirft jedoch spezifische Probleme für die vorderste theoretische Behandlung auf. Ein herausfordernder Aspekt, der kürzlich entdeckt wurde, ist die Existenz multipler Divergenzen der irreduziblen Vertexfunktionen, die in mehreren Vielelektronenmodellen beobachtet wurden. Darunter auch das Hubbard-Modell, gelöst mit der Dynamic Mean Field Theory (DMFT). Für diesen Fall wurde, abhängig von dem untersuchten Gittermodell, eine besondere Diskrepanz im Tieftemperaturverhalten der Vertexdivergenzlinien gefunden. Um zu untersuchen, ob diese Diskrepanz aus dem unterschiedlichen Verhalten des MIT herrührt, werden in der Arbeit die Koexistenzregionen für das Bethe- und das 2D-Quadratgitter analysiert. Dieser Vergleich zeigt auch den Einfluss der Form der Zustandsdichte (DOS) auf die MIT. Für die numerischen DMFT Rechnungen wurde das *w2dynamics*-paket verwendet, das eine effiziente Implementierung eines zeit kontinuierlichen Quanten-Monte-Carlo Verunreinigungslösers darstellt. Für beide Gitter wird die Selbstenergie und die Doppelbesetzung bei unterschiedlichen Temperaturen berechnet. Aus diesen GröSSen werden die kritischen Wechselwirkungswerte U_{c1} und U_{c2} als Funktion der Temperatur erhalten.

Contents

1 Introduction

1.1 Strongly correlated electron systems

Systems with strong interaction between the electrons are called strongly correlated electron systems. The description of such systems is not possible with models which neglect the interaction. Many materials show very interesting properties, due to the correlation among the electrons. The reason for the high interaction is the shape of the orbitals, namely a very narrow shape, which increases the probability for two electrons to be close to each other. So the confinement leads to a high Coulomb interaction, which cannot be neglected. This effect is very significant for the 3d- and 4f-orbitals.

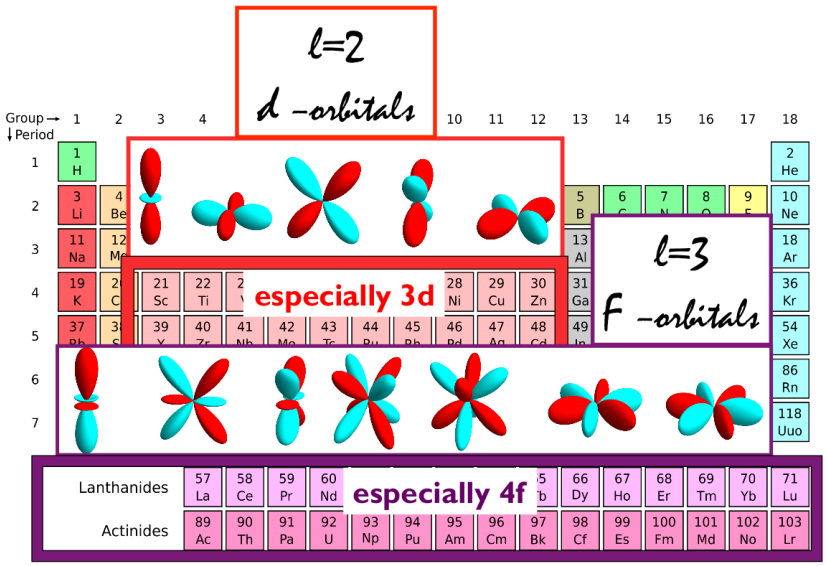

Figure 1: Shapes of the d- and f-orbitals with the elements in 3d- and 4f-configurations, taken from [1]

1.1.1 Fermi-liquid theory

A higher Coulomb interaction affects the mobility of electrons. This can be described by the Fermi-liquid theory, which uses quasi-particles instead of electrons. For the change from electrons to quasi-particles the concept of adiabatic continuity is used. The starting point is the ground state of the system with one excited electron and no interaction. In an adiabatic manner the interaction is turned on, thus the non interacting eigenstates are changing to

eigenstates of the interacting system. The quantum numbers can be assumed to stay the same, where else the energy and the wave-function are changing. However the consequence is a one-to-one correspondence between the free electrons and the quasi-particles. The lifetime equals the Eq. (1), i.e. the lifetime diverges at $T = 0$ at the Fermi surface and decreases quadratically for finite temperatures per energy. In other words, this concept works only close to the Fermi-surface and at low temperatures w.r.t. the Fermi-temperature.

$$\frac{1}{\tau_{\vec{k}}} \propto (\varepsilon_{\vec{k}} - \varepsilon_F)^2 \tag{1}$$

The change of the energy though the interaction is reflected in the mass of the quasi-particles, which is called the effective mass m^*. m^* and also the movement are connected to the dispersion relation $\varepsilon_{\vec{k}}$ given by Eq. (2).

$$\vec{v}\left(\vec{k}\right) = \frac{1}{\hbar}\nabla_{\vec{k}}\varepsilon_{\vec{k}} = \frac{\hbar\vec{k}}{m^*}, \quad |\vec{k}| \sim k_F \tag{2}$$

Physically an electron „carries“ other electrons through the interaction. So the electrons have a different speed and that can be described with a free electron movement with a different mass. For a more detailed description see [2]. In our case the self-energy $\Sigma(i\omega_n)$ is the connection to the quasi-particle properties (see section 2.2.1). As a result of the kinetic energy and the interaction, strongly correlated electron systems are difficult to describe. One model describing these systems is the Hubbard-model.

1.1.2 Hubbard model

The Hubbard model is used for the description of quantum many-body systems [3]. In the simplest realization, this model considers the electron hopping between neighboring lattice sites and the Coulomb-interaction among electrons on the same lattice site. There are four configurations on one lattice site possible ($|0\rangle$, $|\uparrow\rangle$, $|\downarrow\rangle$ and $|\uparrow\downarrow\rangle$). The Hamiltonian of the Hubbard-model is given in Eq. (3).

$$H = -t \sum_{\langle i,j\rangle,\sigma} c^\dagger_{i\sigma} c_{j\sigma} + \frac{U}{2} \sum_i n_{i\uparrow} n_{i\downarrow} + h.c. \tag{3}$$

The first term in Eq. (3) describes the electron-hopping between lattice sites i and j where t is the hopping integral, $c_{j\sigma}$ is the annihilation and $c^\dagger_{i\sigma}$ is the creation operator. The kinetic energy is given by this term, which can be diagonalized in the momentum space.

The second term describes the Coulomb-interaction between a spin-up and a spin-down electron on lattice site i, which is diagonal in position space and is defining the potential energy. The U in this term corresponds to the strength of the screened Coulomb-interaction and the occupation number operators $n_{i\sigma} = c^{\dagger}_{i\sigma} c_{i\sigma}$ measures the number of electrons with spin σ on lattice site i. The long range behavior of the Coulomb-potential $\left(\frac{1}{r}\right)$ and also other long range effects are neglected. Hence the so called Hubbard U is only local and constant in space. The value of U can be estimated by a Coulomb-integral in a Wannier-basis set and the strength strongly depends on the confinement of the orbitals.

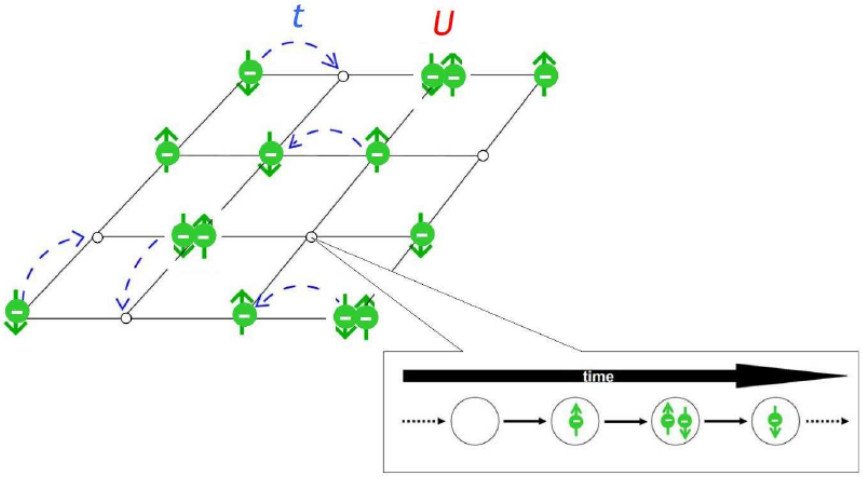

Figure 2: Schematic representation of the Hubbard-model to illustrate the change of states over time. It shows electrons in the solid hopping between lattice sites (hopping: t) and the double occupancy of up-electrons ($\uparrow$) and down-electrons ($\downarrow$) on the same sites (interaction: U). Picture taken from [4]

Besides U and t, the temperature, the dimension of the lattice and the filling are parameters of the Hubbard model. Based on the filling, the density of the electrons $n = n_{\uparrow} + n_{\downarrow}$ can also be used as a parameter. From the Pauli principle it follows that $n_{\sigma} \leq 1$ for $\sigma = \uparrow, \downarrow$ and so $n \leq 2$. A special case is the half filled case, where $n = 1$.
Other special cases are $U = 0$ or $t = 0$. In the case of $U = 0$, the electrons can move freely as Bloch-waves. The case $t = 0$ describes a system without hopping which is called atomic limit. The atomic limit is reached for $U >> t$. Exact solutions for the Hubbard-model are not available, except for the case of one dimension and infinite dimensions. One of the most commonly used methods to approach the model is the dynamical mean-field theory (DMFT).

1.1.3 Dynamical mean-field theory

The Hubbard model can be solved using the dynamical mean-field theory (DMFT). In DMFT the lattice problem is mapped onto a local impurity problem which is solved self-consistently. The idea behind DMFT comes from mean-field treatments of classical problems. An example for that is the Ising-Hamiltonian, which describes localized spins interacting with the surrounding spins. To solve the Ising-Hamiltonian in three dimensions, the surrounding spins are approximated with their average and described by a global Weiss-mean-field. The problem is solved self-consistently until the effective magnetization of the Weiss-field matches with the behavior of the neighboring spins. This description becomes rigorously exact for infinite dimensions, respectively infinitely many neighbors.

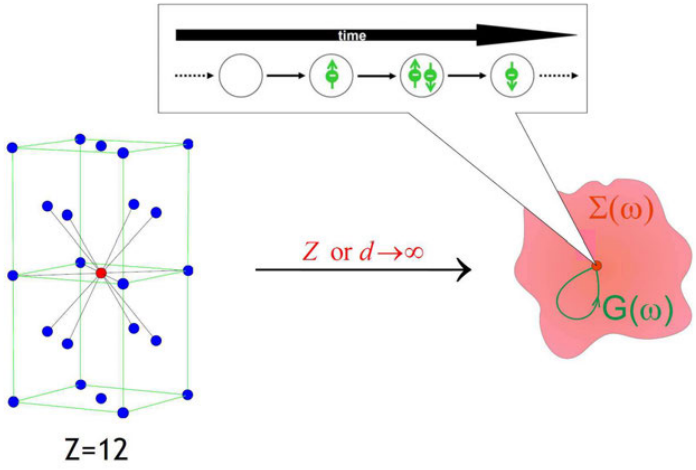

Figure 3: Reduction of the Hubbard-model to a dynamical mean-field in the limit of Z or $d \to \infty$. Electrons can hop onto the single site and back. The electrons can interact on the impurity site. $G(\omega)$ is the local propagator and $\Sigma(\omega)$ is the self-energy of the dynamical mean field, which both are used in the calculations. Picture taken from [4]

The principle behind DMFT is similar. All non-local correlations are averaged out in the limit of infinite dimensions. The dynamics in DMFT comes in because the mean-field in DMFT is a time dependent quantity, the effective Weiss-field $\mathcal{G}_\sigma = \mathcal{G}_\sigma(t)$ or $h_{eff} = h_{eff}(t)$. Thus, the possible states of the single impurity site ($|0\rangle$, $|\uparrow\rangle$, $|\downarrow\rangle$ and $|\uparrow\downarrow\rangle$) are changing over time and so the full dynamics of the problem can be captured. DMFT can describe temporal correlations, but the spatial correlations are lost. The lattice problem in dimension $d \to \infty$ can be mapped onto a single interacting impurity site in

a bath of conduction electrons, hence an Anderson impurity model. To solve this impurity problem several methods are available, in this work CT-QMC (see section 2.1) was used.
The local propagator $G_\sigma(i\omega_n)$ is given by a functional integral over Grassmann variables (4)

$$G_\sigma(i\omega_n) = -\frac{1}{\mathcal{Z}} \int \prod_\sigma Dc_\sigma^\dagger Dc_\sigma [c_\sigma(i\omega_n) c_\sigma^\dagger(i\omega_n)] exp[-S_{loc}] \tag{4}$$

where $\mathcal{Z}$ is the partition function:

$$\mathcal{Z} = \int \prod_\sigma Dc_\sigma^\dagger Dc_\sigma exp[-S_{loc}] \tag{5}$$

and the local action S_{loc} is given in Eq. (6)

$$S_{loc} = -\int_0^\beta \int_0^\beta d\tau d\tau' \sum_\sigma c_\sigma^\dagger(\tau') \mathcal{G}_\sigma^{-1}(\tau' - \tau) c_\sigma(\tau) + U \int_0^\beta n_\uparrow(\tau) n_\downarrow(\tau) \tag{6}$$

Here $\mathcal{G}_\sigma$ is the effective local propagator respectively the bath Green function or Weiss-mean-field.
After solving the AIM problem, the solution is used for the self-consistency equation (7).

$$\Sigma_\sigma(i\omega_n) = \mathcal{G}_\sigma^{-1}(i\omega_n) - G_\sigma^{-1}(i\omega_n) \tag{7}$$

The self-consistency equation yields the self-energy $\Sigma_\sigma(i\omega_n)$, which is used to calculate the lattice Greens function G_{loc} as shown in equation (8).

$$G_{loc}(i\omega_n) = \sum_{k \in BZ} \frac{1}{i\omega_n - \varepsilon_k + \mu - \Sigma_\sigma(i\omega_n)} \tag{8}$$

That lattice Green function is, then used to calculate a new Weiss-mean-field (9)

$$\mathcal{G}_\sigma^{-1}(i\omega_n) = G_{loc}^{-1}(i\omega_n) + \Sigma_\sigma(i\omega_n) \tag{9}$$

In DMFT, starting with an initial guess e.g. for $\Sigma_\sigma(i\omega_n)$, this DMFT-cycle is running until the requirement $G_{loc}(i\omega_n) = G_\sigma(i\omega_n)$ is fulfilled. The DMFT-cycle is mapped in Fig. 4 and for more details see [6] or [4].

1.1.4 Mott-Hubbard metal-insulator-transition

One of the most famous and intriguing phenomena in strongly correlated electron systems is the Mott-Hubbard-transition or metal-insulator-transition

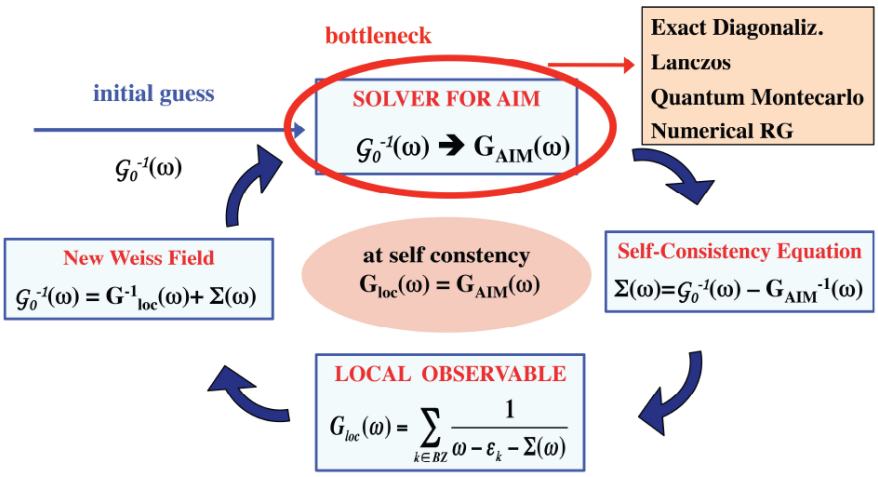

Figure 4: The DMFT cycle, taken from [7]

(MIT). It describes a first order phase transition between a paramagnetic metal (PM) and a paramagnetic insulator (PI). This type of transition is completely different from the transition between metals and band insulators, which arises from the band filling of the electrons. The MIT is connected to the correlation effects of strongly correlated electrons. It can be explained through the decreasing probability of the double occupancy by an increasing Coulomb-interaction U in the Hubbard-model. For higher interactions the energy costs for two electrons to be on the same lattice site increases. However the total energy of the system can be reduced by localizing the electrons. Thus, after a critical interaction value is reached, the metal becomes a paramagnetic insulator.

Fig. 5 shows the splitting of the density of states (DOS), i.e. the formation of the Hubbard bands, and the emergence of the band gap, depending on U scaled with the band-width W. The DOS of the non-interacting system (a) converts to a three-peak-structure (c) with increasing U. This depends on a splitting of the local propagator $G_\sigma(i\omega_n)$ in an incoherent part, which is responsible for the two peaks beside the Fermi-energy ($E_F \pm \frac{U}{2}$), and a coherent part at E_F. The width of the coherent peak is proportional to the quasi-particle weight Z and moreover $Z \propto \frac{1}{m^*}$. For larger U the peak disappears (d) thereby $Z = 0$ and $m^* \rightarrow \infty$. Thus the mobility of the electrons vanishes and the system shows an insulating behavior.

A typical phase-diagram is shown in Fig. 6. The region inside the borders of the MIT phases is called the coexistence region, where both phases (PM and PI) can exist. The coexistence region is located at low temperatures between

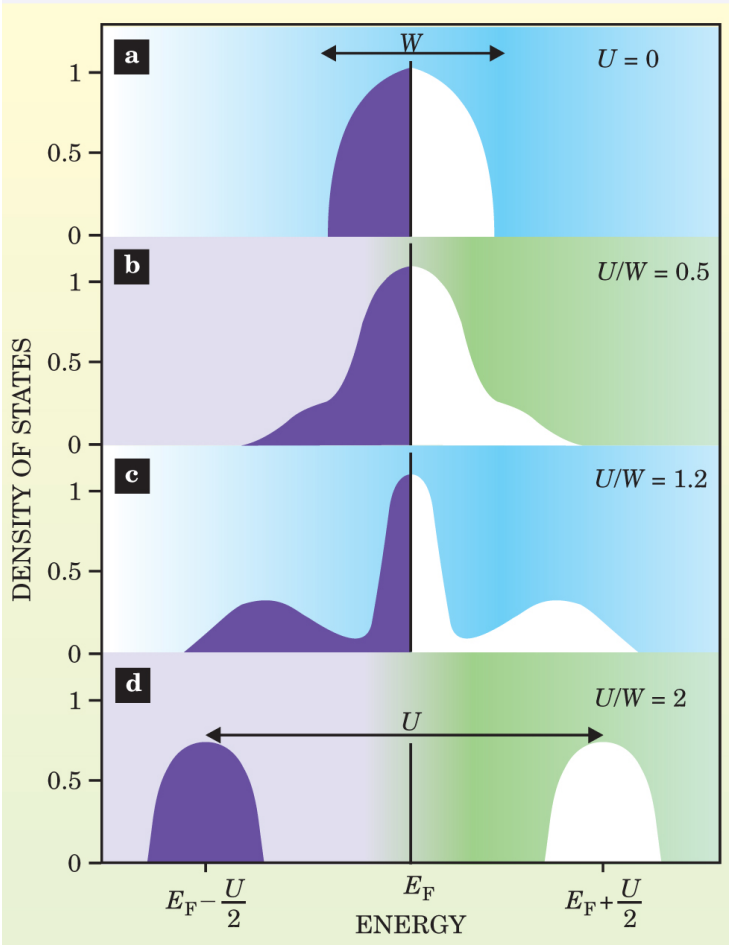

Figure 5: Change of the density of states depending on the Hubbard U, taken from [8]

the critical values on the metallic side U_{c1} and on the insulating side U_{c2}. The point where U_{c1} and U_{c2} are crossing is the critical end point. At this point the system has a second order transition. The real first order transition line (dashed line) in the coexistence region is obtained by analyzing the minimum of the free energy. It proceeds from the critical end point downwards and bends slightly towards the U_{c2} line, because the U_{c2} line has a second order transition at $T = 0$.

1.2 Motivation

Recent studies have shown that irreducible vertex divergences occur in several models for strongly correlated electrons, such as the half-filled two-

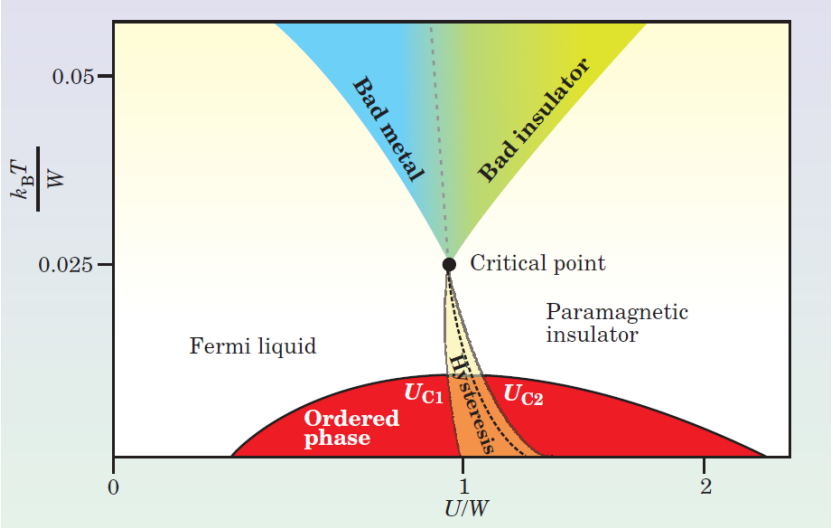

Figure 6: Typical structure of a MIT phase diagram, taken from [8]

dimensional Hubbard model, solved by means of DMFT [9], [10]. For this case the corresponding phase-diagram and the irreducible divergence lines are shown in the left panel of Fig. 7.
One finds multiple divergence lines surrounding the MIT, where the different colors of divergence lines corresponds to the two distinct kinds of divergences appearing in specific physical scattering channels (red: charge Γ_c, orange: charge Γ_c and particle-particle up-down $\Gamma_{pp,\uparrow\downarrow}$ simultaneously). In the region of high T and large U the divergences in the Hubbard model are approximated well by those of the Hubbard atom. On the other side the lines are bending rightwards when the metallic behavior of the system increases. Because of this the lines get for $T \to 0$ finite values of U, which are dependent on the density of states. The reason of this behavior at low temperatures is not known yet. In particular the right panel of Fig. 7 shows the first divergence line at low temperature for the Bethe-lattice and the 2D-square-lattice. The motivation for this work is to compare the phase-diagrams for these two lattices in particular the behavior of the corresponding MIT's. Due to the huge difference in the density of states of the two lattices a distinct behavior of the low temperature coexistence regions of the corresponding MIT's can be expected. In this case the difference in the low T behavior of the divergence lines might be attributed to that.

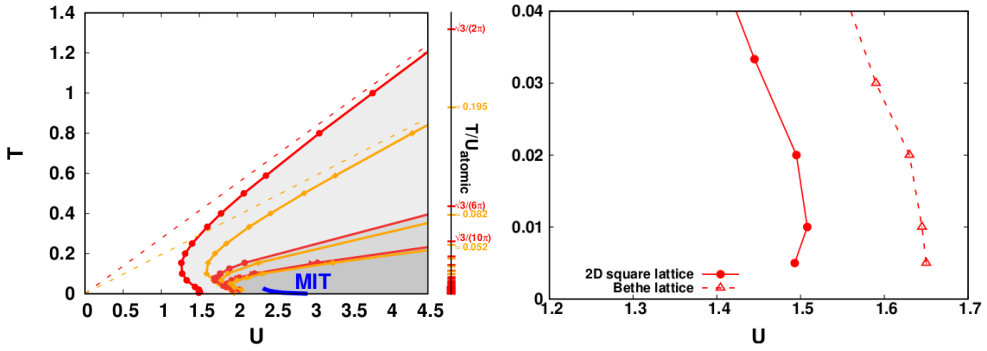

(a) DMFT phase-diagram with the lines surrounding the MIT in the half-filled square-lattice Hubbard model

(b) First divergence line for the 2D square lattice (solid line) and the Bethe lattice (dashed line) at low temperature.

Figure 7: Irreducible vertex divergences in the Hubbard model solved by DMFT, pictures taken from [9]

1.2.1 Density of states

In this thesis, the Hubbard model is solved in DMFT using CT-QMC methods implemented in the *w2dynamics* package (see section 2.1). As a starting point the non-interacting density of states (DOS) is needed. The following sections show the non-interacting DOS for the two lattices.

Bethe-lattice DOS

The Bethe-lattice DOS has a simple form, allowing sometimes analytic calculations, which is why it is widely used in theoretical solid-state physics. This DOS has a semi-elliptic shape (see Fig. 8) and is given in Eq. (10), [11]. A band-width of $W = 2$ implies a hopping integral value of $t = \frac{1}{2}$.

$$D_{bethe}(\varepsilon) = \frac{1}{2\pi t^2}\sqrt{4t^2 - \varepsilon^2} = \frac{4}{\pi W^2}\sqrt{W^2 - 4\varepsilon^2} \tag{10}$$

Square-lattice DOS

The DOS of the square-lattice is constructed by the eigenvalues of the non-interacting Hubbard-Hamilton (Eq. (3)). To get the eigenvalues we consider the case of an one-dimensional tight-binding lattice. The non-interacting part of the Hubbard-Hamilton, considering only the hopping between the nearest neighbors is given in Eq. (11).

$$H = -t\sum_{j,\sigma}\left(c^\dagger_{j-1,\sigma}c_{j,\sigma} + c^\dagger_{j+1,\sigma}c_{j,\sigma}\right) \tag{11}$$

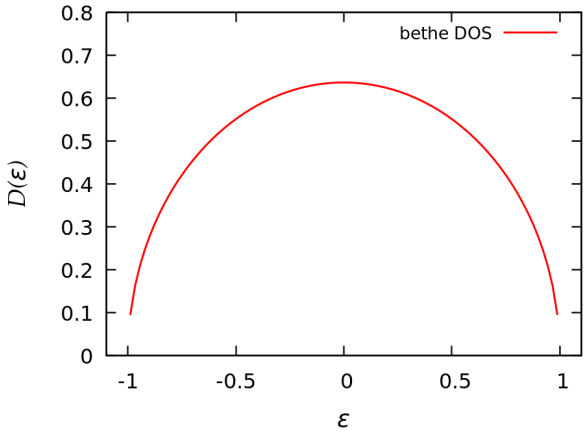

Figure 8: The semi-elliptic Bethe-lattice density of states given by Eq. (10)

Here the lattice site index is $j = 0, 1, 2, , N$ and the location of the lattice site is given by $x_j = ja$, with the lattice constant a. The total length of the lattice is $L = Na$ and the basis transformation to the momentum space is given by Eq. (13).

$$c^\dagger_{j,\sigma} = \frac{1}{\sqrt{L}} \sum_{k,\sigma} e^{ikx_j} c^\dagger_{k,\sigma} \tag{12}$$

$$c_{j,\sigma} = \frac{1}{\sqrt{L}} \sum_{k',\sigma} e^{-ik'x_j} c_{k',\sigma} \tag{13}$$

The periodic boundary condition $x_0 = x_N$ implies $k = \frac{2\pi}{L} j$. Assuming $k' = k + G$ and $j' = j + 1$, $k + G = \frac{2\pi}{L}(j+1)$ takes effect, G is here a reciprocal lattice vector. So the annihilation and creation operators for each lattice site can be reduced to the first Brillouin zone.

$$\begin{aligned} c_{j,\sigma} &= \frac{1}{\sqrt{L}} \sum_{k',\sigma} e^{-ik'x_j} c_{k',\sigma} = \frac{1}{\sqrt{L}} \sum_{k+G,\sigma} e^{-i(k+G)x_j} c_{k+G,\sigma} = \\ &= \frac{1}{\sqrt{L}} \sum_{k+G,\sigma} e^{-ikx_j} e^{iGx_j} c_{k+G,\sigma} = \\ &= \left| Gx_j = jGa = j2\pi \ , \quad c_{k+G,\sigma} \equiv c_{k,\sigma} \right| = \\ &= \frac{1}{\sqrt{L}} \sum_{k,\sigma} e^{-ikx_j} c_{k,\sigma} \end{aligned} \tag{14}$$

Thus we get the Hamiltonian (Eq. (11)) in the momentum space and thereby the eigenvalues ε_k, where $c^\dagger_{k,\sigma}c_{k,\sigma}$ is the occupation number operator $n_{k,\sigma}$.

$$\begin{aligned} H_{k,\sigma} &= -t\sum_{x_j,\sigma}^{L}\left(\frac{1}{L}\sum_{k,\sigma}e^{ika(j-1)}e^{-ikaj}+\frac{1}{L}\sum_{k,\sigma}e^{ika(j+1)}e^{-ikaj}\right)c^\dagger_{k,\sigma}c_{k,\sigma} = \\ &= -t\sum_{k,\sigma}\Big(e^{-ika}+e^{ika}\Big)n_{k,\sigma} = -2t\sum_{k,\sigma}cos\Big(ka\Big)n_{k,\sigma} \end{aligned} \tag{15}$$

$$\Rightarrow \quad \varepsilon_{\vec{k}} = -2tcos\Big(ka\Big) \tag{16}$$

The eigenvalues of the square-lattice are identical, up to the additional dimension, which yields

$$\varepsilon_{\vec{k}} = -2t\Big[cos\Big(k_xa\Big)+cos\Big(k_ya\Big)\Big] \tag{17}$$

To calculate the DOS of the square-lattice Eq. (18) is used.

$$D(\varepsilon) = \frac{1}{L^d}\sum_{\vec{k}}\delta(\varepsilon-\varepsilon_{\vec{k}}) \tag{18}$$

This sum over the delta distributions with the eigenvalues of the square-lattice is only numerically solvable. So the delta distribution must be replaced by a numerically usable approximation, in our case the Lorentzian form $\delta_\Delta(x) = \frac{1}{\pi}\frac{\Delta}{x^2+\Delta^2}$, with $\lim\limits_{\Delta\to 0}\delta_\Delta(x) = \delta(x)$. In this case, the expression for the DOS reads as follows:

$$D_{square}(\varepsilon) \simeq \frac{1}{(Na)^2}\sum_{k_x}^{N}\sum_{k_y}^{N}\frac{\Delta}{\pi}\left\{\left[\varepsilon+2t\Big[cos\Big(k_xa\Big)+cos\Big(k_ya\Big)\Big]\right]^2+\Delta^2\right\}^{-1} \tag{19}$$

The number of wave vectors N and the width of the Lorentzian form Δ are parameters of the numerical solution. The precision increases for increasing N and decreasing Δ. As a first guess for Δ the value of the imaginary part of a self-energy for the Bethe-lattice at $i\omega_n = 0$ and temperature $\beta = 200$ is used. Polynomials in several intervals and of different orders are used for the fitting of $Im[\Sigma(i\omega_n)]$. These polynomials are given in the following and plotted in Fig. 9.

- $p_1(x) = a_1 + b_1x \quad with \quad x \in [0, 0.05]$
- $p_2(x) = a_2 + b_2x + c_2x^2 \quad with \quad x \in [0, 0.1]$
- $p_3(x) = a_3 + b_3x + c_3x^2 \quad with \quad x \in [0, 0.2]$

- $p_4(x) = a_4 + b_4 x + c_4 x^2 + d_4 x^3 \quad with \quad x \in [0, 0.2]$
- $p_5(x) = a_5 + b_5 x + c_5 x^2 + d_5 x^3 \quad with \quad x \in [0, 0.3]$
- $p_6(x) = a_6 + b_6 x + c_6 x^2 + d_6 x^3 \quad with \quad x \in [0, 0.4]$
- $p_7(x) = a_7 + b_7 x + c_7 x^2 + d_7 x^3 + e_7 x^4 \quad with \quad x \in [0, 0.2]$
- $p_8(x) = a_8 + b_8 x + c_8 x^2 + d_8 x^3 + e_8 x^4 \quad with \quad x \in [0, 0.3]$
- $p_9(x) = a_9 + b_9 x + c_9 x^2 + d_9 x^3 + e_9 x^4 \quad with \quad x \in [0, 0.4]$

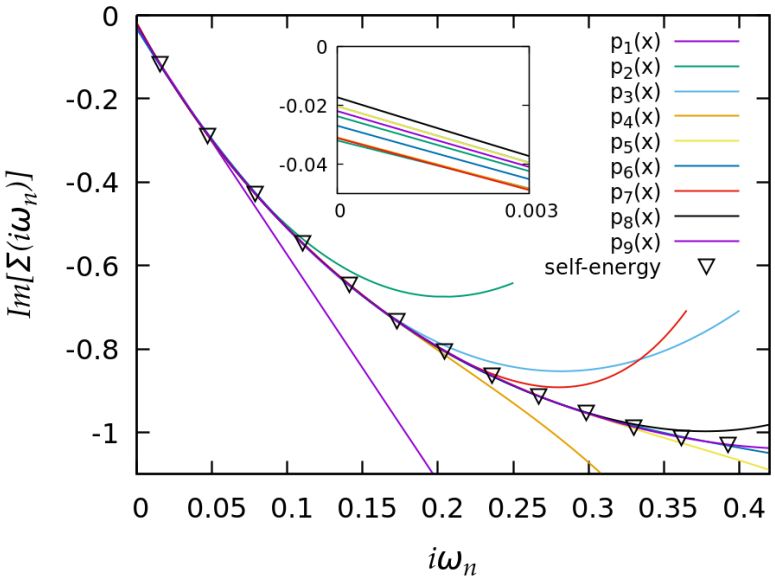

Figure 9: Imaginary part of the self-energy $\Sigma(i\omega_n)$ of the Bethe-lattice at $\beta = 200$ approximated by polynomials for an estimation of the scattering rate γ, which is needed for the square-lattice DOS calculation.

The insert of Fig. 9 shows the value of $Im[\Sigma(i\omega_n = 0)] \sim 0.025$, which is a guess for the maximal Δ. The value of N is set to a value, such that the numerical solution for $\Delta < 0.025$ results in a smooth function. The square-lattice DOS calculated with Eq. (19) is shown in Fig. 10, for two sets of parameters Δ and N, showing the big difference between the two DOS. In contrast to the semi-elliptic shape of the Bethe-lattice DOS, the square-lattice DOS has a Van-Hove-singularity, which is located where the dispersion relation $\varepsilon_{\vec{k}}$ has an extremum, i.e. where $|\vec{\nabla}\varepsilon_{\vec{k}}| = 0$.
In our case we set $N = 1000$, to save computing time whereas the value of

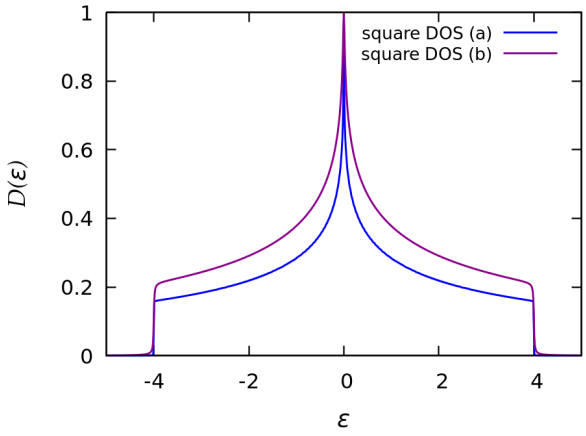

Figure 10: Square-lattice density of states numerically calculated by Eq. (19), showing a logarithmic divergence at $\varepsilon = 0$. (a) uses $\Delta = 0.001$ and $N = 3000$, (b) $\Delta = 0.01$ and $N = 1000$

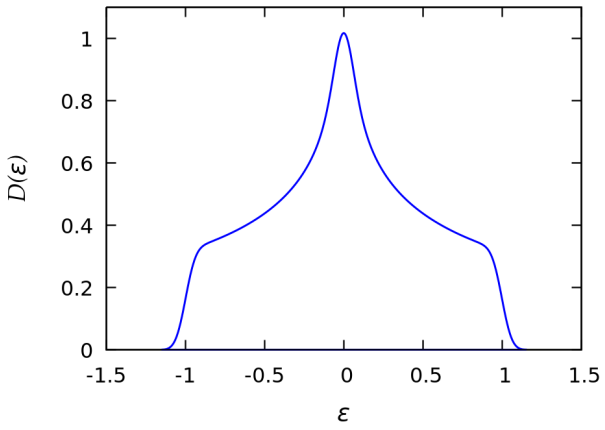

Figure 11: Square-DOS calculated by *w2dynamics*, and exploited for the DMFT calculations. Note the presence of the central peak, which would be associated for infinite resolution ($N \to \infty$) to a Van Hove singularity.

$\Delta = 10^{-10}$. The resulting DOS of the square lattice is shown in Fig. 11.

2 Methods and Calculation

This chapter gives a short overview of the methods exploited to obtain the $U_{c1}(T)$ and $U_{c2}(T)$ lines for both lattices discussed in this thesis. In particular, we will present results for the self-energy and the double occupancy. Eventually, the corresponding phase-diagrams of the two lattices will be shown.

2.1 CT-QMC

CT-QMC (Continuous-time quantum Monte Carlo) is a numerical method to solve the impurity problem. That is the bottleneck of any DMFT cycle. The Hamiltonian of the problem is separated into two terms, where one is exactly solvable and the other is expanded into the interaction part (CT-INT) or the hybridisation part (CT-HYB). The different expansions need different algorithmic descriptions (refer to recent literature [4] [6] and [11]).
In this Bachelor thesis the CT-HYB implementation of the *w2dynamics* [12], [13] has been used. At the center of this work is a single-band Hubbard model with a finite bandwidth set to $W = 2$. In these two cases this also ensures, that the variance of the non-interacting DOS is the same. To enforce a half-filled band, which will be considered in this thesis, the chemical potential is set to $\mu = \frac{U}{2}$.

2.2 Self-energy and double occupancy

The main work of this bachelor thesis is the calculation of the DMFT phase-diagrams for the two different lattice models considered. To achieve this goal several calculations were performed, in particular of the self-energy $\Sigma(i\omega_n)$ and the double occupancy $d = \langle n_\uparrow n_\downarrow \rangle$, because their properties identify the corresponding phase of the system.

2.2.1 Self-enegry

The self-energy $\Sigma(i\omega_n)$ is defined by the Dyson Eq. (7), for more details see section 1.1.3. The imaginary part of $\Sigma(i\omega_n)$ indicates whether the system is in the metallic or the insulating phase. This information is encoded in the behavior of positive, low Matsubara frequencies. Fig. 12 shows the two qualitatively different behaviors of the self-energy.
Physically, the self-energy is related to the mobility of the quasi-particles of the strongly correlated electron system. Through an expansion of the self-energy one obtains quantities, which are related to physical properties, e.g.

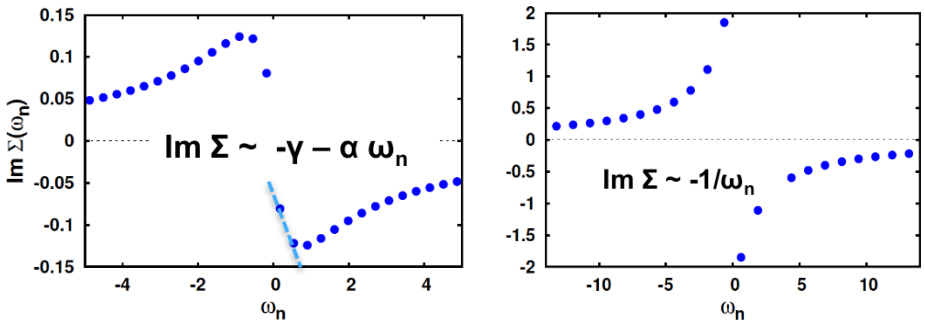

(a) Metallic behavior (b) Insulating behavior

Figure 12: Behavior of the self-energy for the different phases (left: metallic; right: Mott-insulating) of the Hubbard model, pictures taken from [1]

for the metallic case $Im[\Sigma(i\omega_n)] \sim -\gamma - \alpha\omega_n$. The value γ represents the scattering rate and is related to the inverse lifetime τ of the quasi-particles. The slope α in the second term defines the effective mass m^* (see section 1.1.1). For an insulating behavior $Im[\Sigma(i\omega_n)] \sim -\frac{1}{\omega_n}$ holds, which yields vanishing lifetime $\tau = 0$ and thus, no free quasi-particles. For more details see [11].

The procedure to obtain a converged result for the self-energy is described briefly in the following. First, the convergence of the DMFT cycle is reached by performing the calculations with a low relatively statistical precision (Fig. 13).

Once the DMFT convergence is found, only a few iterations are made with a higher precision to reduce the statistical error. This procedure can be repeated for different interaction values U, taking into account a previous converged calculation with low statistical error at the same T and a very close interaction value. In this way a large range of interaction values is scanned for a given temperature. Starting from low interaction values, a metallic behavior is observed, where parameters γ and α are increasing with increasing U. This reflects that the system becomes, gradually, a poorer conductor. When $U = U_{c2}(T)$ is reached, the behavior of $\Sigma(i\omega_n)$ changes dramatically: This is shown in Fig. 14 for $\beta = 200$.

When an interaction value $U > U_{c2}$ is reached the self-energy shows an insulating behavior (orange points in Fig. 14). The self-energies for U values around the critical interaction U_{c2} for $\beta = 200$ are shown in Fig. 15. The phase-diagram can be obtained by analyzing several temperatures T thus way.

Fig. 16 shows analogously to Fig. 14 and Fig. 15 the self-energy for different

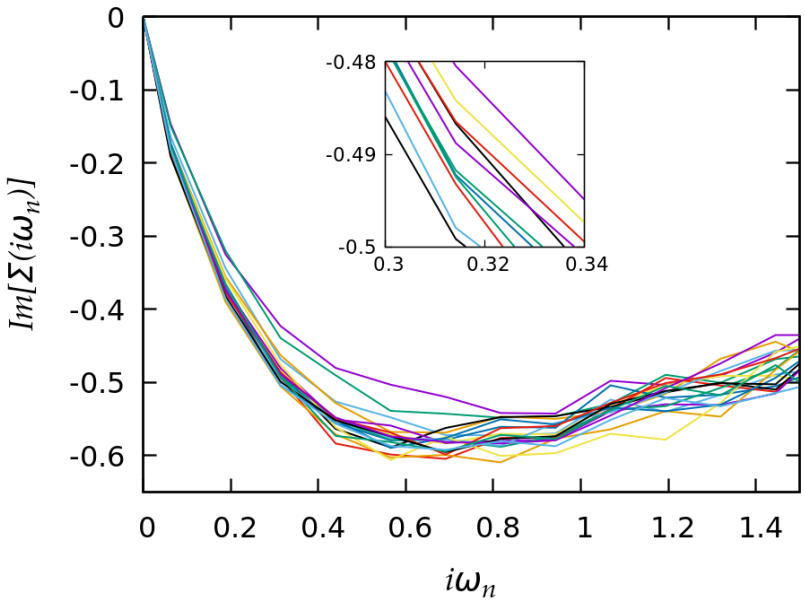

Figure 13: Imaginary part of the self-energy $\Sigma(i\omega_n)$ for several DMFT iterations, showing the convergence of the DMFT cycle on the metallic side at $U = 2.0$ and $\beta = 50$ for the Bethe-lattice. Inset: Converged iterations with small offsets between the calculations

interaction values, however the interaction is now decreasing. This evokes that the system changes from an insulator to a metal, which happens at the critical interaction value $U = U_{c1}(T)$. Note that because of the first order nature of the phase transition it applies $U_{c1}(T) \neq U_{c2}(T)$ (with the exception of the critical endpoints). From an algorithmic perspective, for obtaining the insulating solution in the coexistence region, it is crucial to take into account previous converged calculation, because the stability of the metallic phase is typically greater. [1]

[1]Note that, the value of the mixing parameter for the DMFT self-consistency is bigger. (mixing parameter for metal: 0.6 and insulator: 0.95)

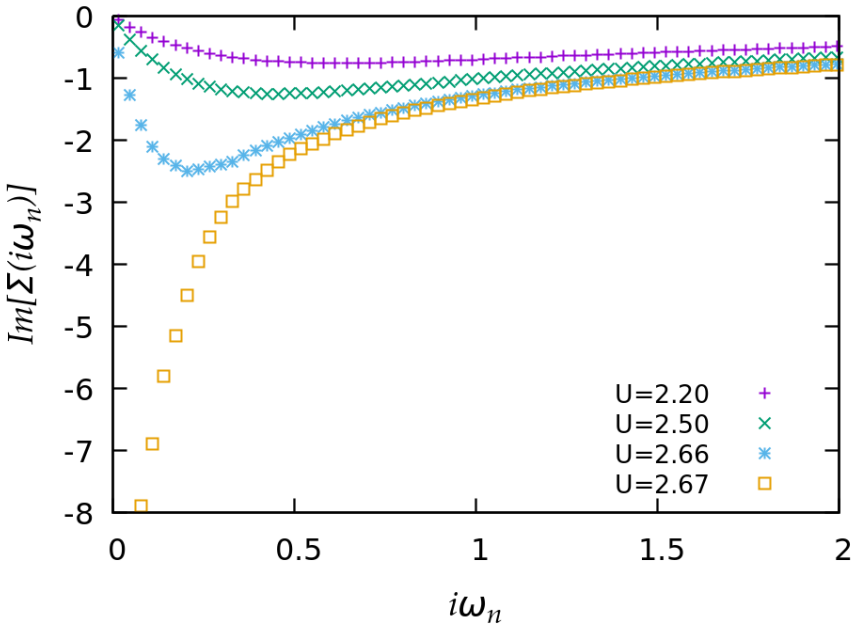

Figure 14: DMFT self-energy $\Sigma(i\omega_n)$ for the Bethe-lattice for $\beta = 200$ and different interactions values U, corresponding to metallic ($U = 2.20, 2.50, 2.66$) and insulating ($U = 2.67$) solutions.

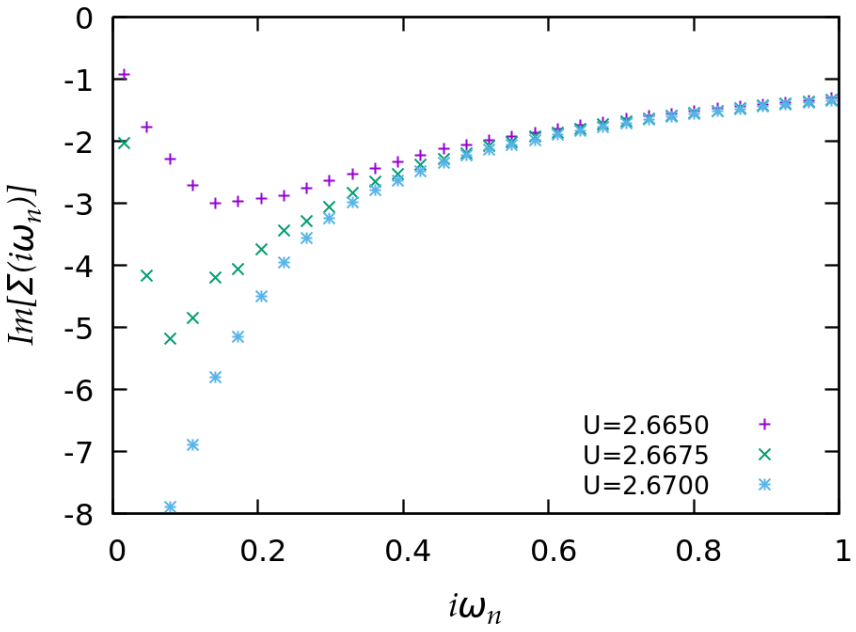

Figure 15: Same as Fig. 14 with a finer resolution in U around U_{c2} (~ 2.6675) for the Bethe-lattice at $\beta = 200$.

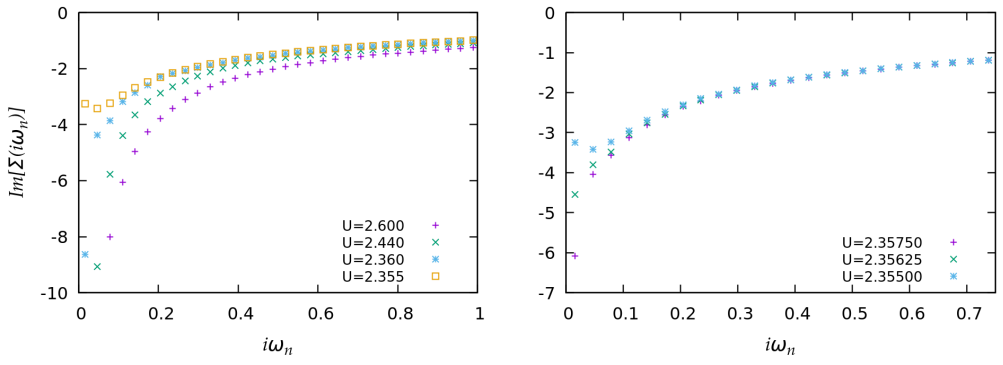

(a) U corresponding to metallic ($U = 2.355$) and insulating ($U = 2.360, 2.440, 2.600$) solutions

(b) U around U_{c1}

Figure 16: DMFT self-energy $\Sigma(i\omega_n)$ for the Bethe-lattice for $\beta = 200$ and different interactions values U

2.2.2 Double occupancy

The other parameter analyzed in this work is the double occupancy $d = \langle n_\uparrow n_\downarrow \rangle$, which is relevant for the identification of the different phases around the MIT and in the coexistence region. It is the expectation value of finding a spin-up and spin-down electron on the same lattice site. This measures the average number of double occupied sites associated to an energy cost equal to U: d is proportional to the potential energy of the system $E_{pot} = \langle H_{pot} \rangle = U \langle n_\uparrow n_\downarrow \rangle = Ud$. For a high interaction U, double occupancies are energetically unfavorable and therefore suppressed. In our case, we consider lattices at half-filling, i.e. $n = n_\uparrow + n_\downarrow = 1$. This implies that the maximum of the double occupancy is $\langle n_\uparrow n_\downarrow \rangle = \langle n_\uparrow \rangle \langle n_\downarrow \rangle = \frac{1}{4}$ at $U = 0$, where the system is uncorrelated. On the other hand, for the limit $U \to \infty$ the double occupancy approaches 0. Physically, it is easy to understand that in the metallic phase the double occupancy is higher than for the insulating phase, because of the larger mobility of the electrons, which corresponds in average to a higher possibility of finding two electrons on the same lattice site.

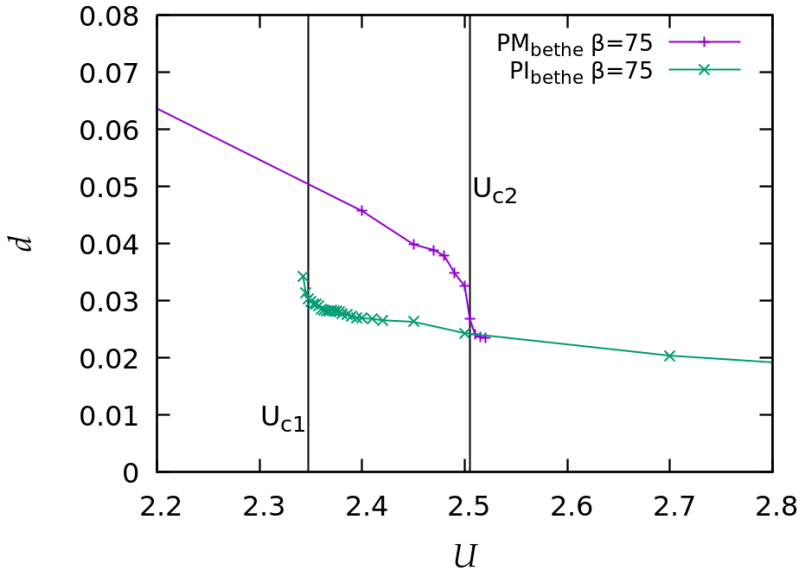

Figure 17: Expectation value of the double occupancy $d = \langle n_\uparrow n_\downarrow \rangle$ as a function of the interaction U at $\beta = 75$ for the Bethe-lattice

The DMFT results for the double occupancy as a function of the interaction U is shown in Fig. 17 for the Bethe-lattice at temperature $\beta = 75$, for two data sets. The purple set shows the calculations, where U was increased

starting from a metallic solution. Opposed to that the green set represents the results for decreasing interaction values, starting from an insulating solution. The area where the results of the two data sets are different is the coexistence region. There, the metallic and the insulating phase are found simultaneously, reflecting the typical hysteresis of the first order MIT. The corresponding critical interaction values U_{c1} and U_{c2} are shown as well, taken from the analysis of the behavior of the self-energy (see section 2.2.1). In general, we observe a significant difference between the two data sets. More in detail: for the purple data sets the double occupancy drops continuously with the decreasing U and at U_{c2} the double occupancy is quite close to double occupancy on the other data set. For the green data set the double occupancy increases only very weakly for decreasing U until an abrupt change is observed at U_{c1}.

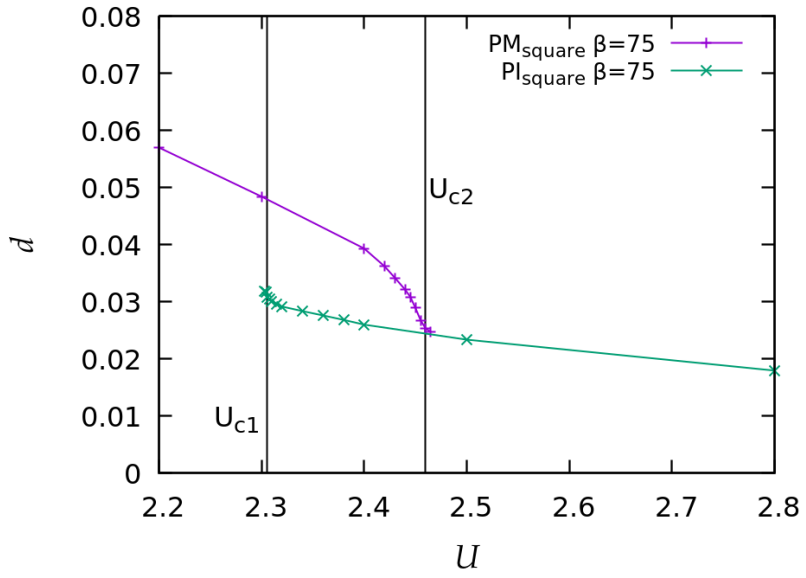

Figure 18: Expectation value of the DMFT double occupancy $d = \langle n_\uparrow n_\downarrow \rangle$ as function of the interaction U at $\beta = 75$ for the square-lattice

The calculations for the square-lattice, shown in Fig. 18 are qualitatively similar to the ones of the Bethe-lattice. A quantitative difference is found, however, for the location in parameter space of the coexistence region. For the square-lattice the critical interactions U_{c1} and U_{c2} are slightly smaller although the overall width of the coexistence region remains nearly equal. This happens for all temperatures considered in this work. Fig. 19 shows the comparison for $\beta = 40$, close to the critical endpoint and Fig. 20 for the

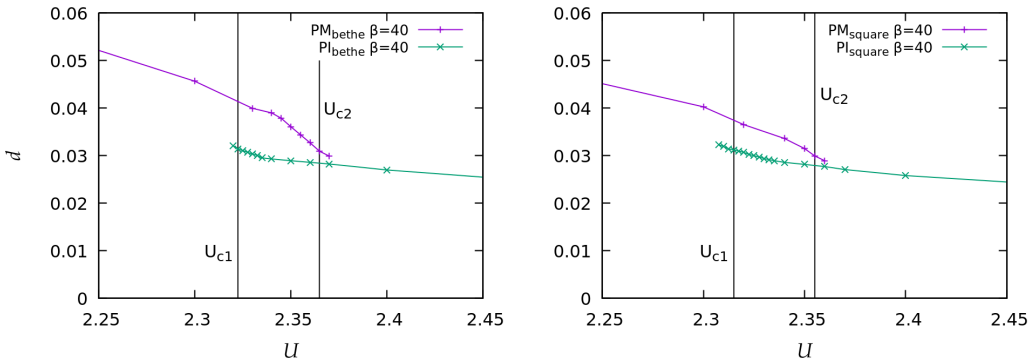

(a) bethe-lattice

(b) square-lattice

Figure 19: Expectation value of the double occupancy $d = \langle n_\uparrow n_\downarrow \rangle$ for the two lattice models and different values of the interaction U at $\beta = 40$

lowest temperature calculated ($\beta = 200$).
As a general trend, we observe that the coexistence region gets continuously broader with decreasing temperature. At the temperature of the critical endpoint ($\beta \sim 33$), the data sets of the double occupancy merge, displaying a kink at the critical U, while for the temperatures above it d is a continuous function for all U.

Let us note that the CT-QMC calculations do not always preserve particle-hole symmetry. This can be ascribed to a non-ergodicily of the DMFT calculation for the insulating solution. The violation is stronger for lower temperatures. As an example in Fig. 21, $G(\tau)$ is composed with itself mirrored around $\tau = \frac{\beta}{2}$, which should not yield any difference. This has, however, no influence on the results for the self-energy or the double occupancy (at least for the precision level required by our analysis) meaning that it does not affect the conclusions presented in this thesis.

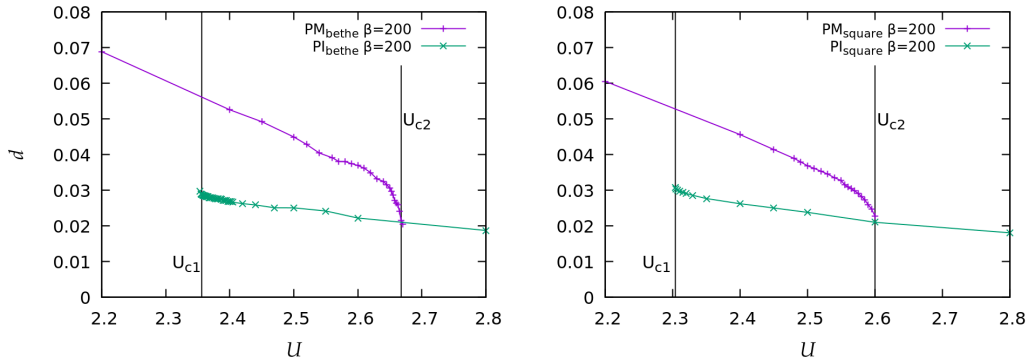

(a) bethe-lattice (b) square-lattice

Figure 20: Expectation value of the double occupancy $d = \langle n_\uparrow n_\downarrow \rangle$ for the two lattice models and different values of the interaction U for calculations at the lowest temperature $\beta = 200$

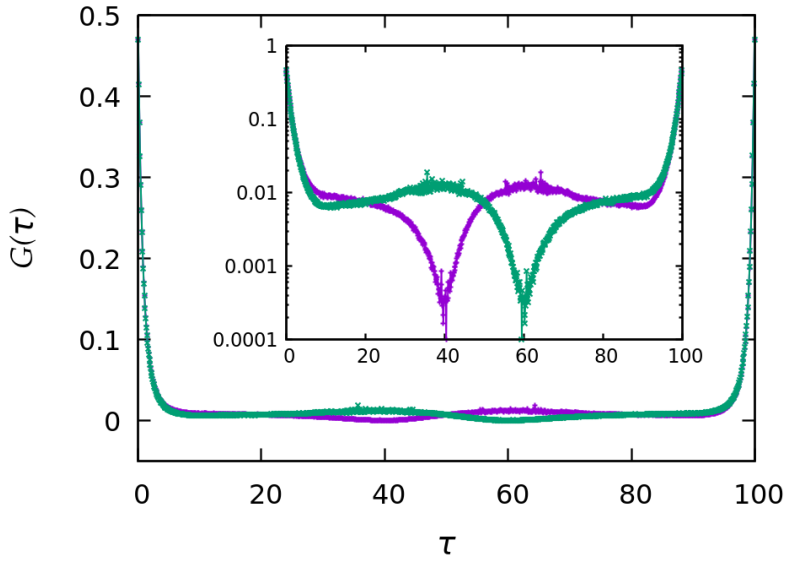

Figure 21: Local propagator $G(\tau)$ for $U = 2.55$ at $\beta = 100$ on the insulating side. Inset: Same plot on a logarithmic scale.

2.3 Phase-diagram of the Bethe-lattice

We can summarizing the results of our DMFT calculations described in section 2.2, by plotting the corresponding phase-diagram of the Bethe-lattice, shown in Fig.22.

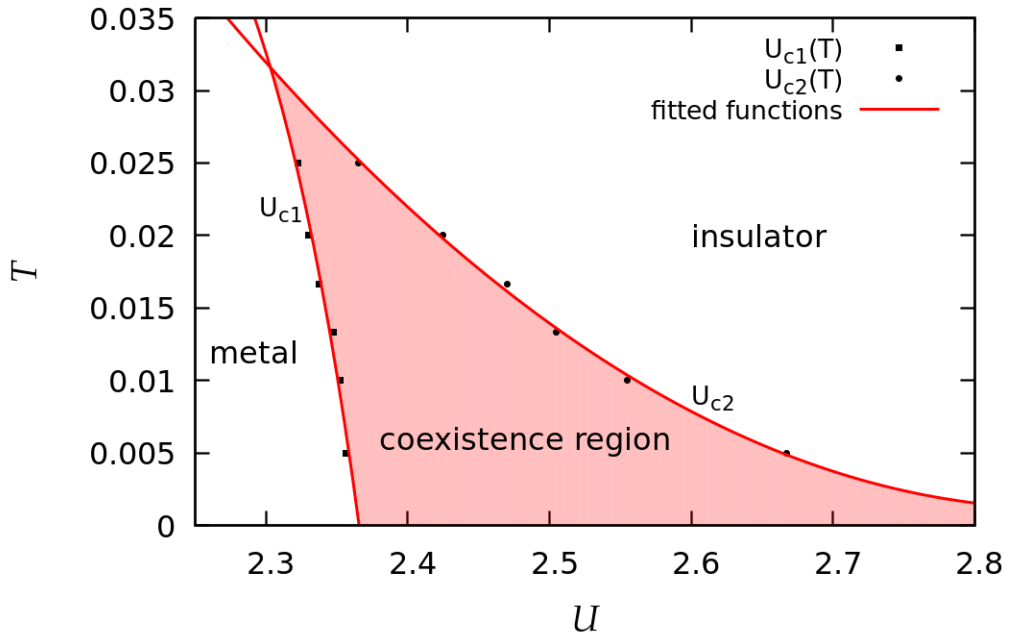

Figure 22: DMFT phase-diagram of the half-filled Hubbard model on a Bethe-lattice

The diagram shows the MIT as a function of the temperature T and the interaction U in units of the half-bandwidth $\frac{U}{2W}$. The data sets $U_{c1}(T)$ and $U_{c2}(T)$ were fitted using *gnuplot* with the following fitting functions

- $f_1(x) = a_1 + b_1 x^{c_1} \quad for \quad U_{c1}$
- $f_2(x) = a_2 + b_2 x + c_2 x^2 \quad for \quad U_{c2}$

Fig. 22 shows the increase of both critical interactions ($U_{c1}(T)$, $U_{c2}(T)$) with decreasing temperature and as well an approximated estimate for the position of the critical endpoint, where the $U_{c1}(T)$ and $U_{c2}(T)$ lines merges. In the phase-diagram the different phases of the Hubbard model are also shown with a coexistence region broadening with decreasing temperature.

2.4 Phase-diagram of the 2D-square-lattice

Analogously we have also obtained the DMFT phase-diagram for the Hubbard model on a square lattice, shown in Fig. 23.

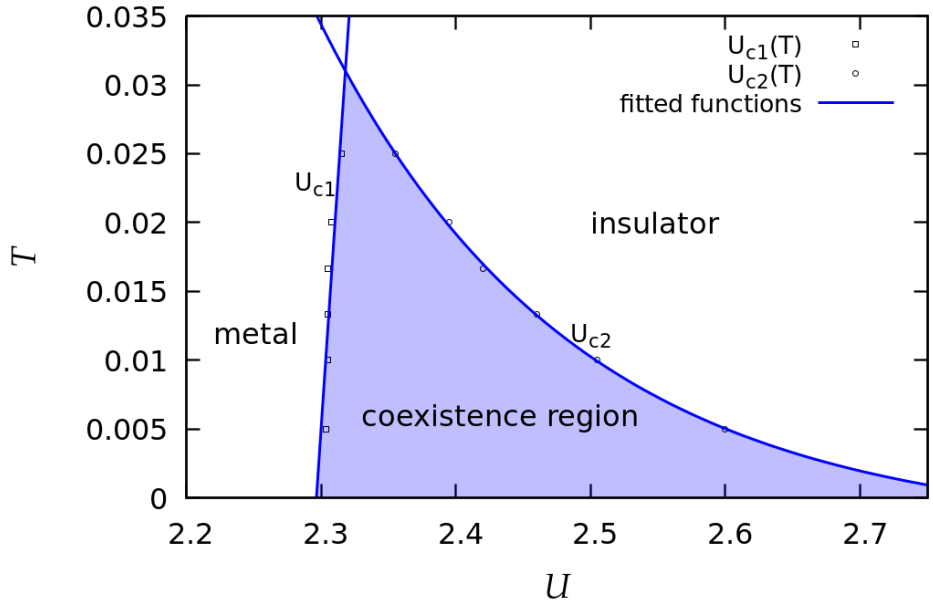

Figure 23: DMFT phase-diagram of the half-filled Hubbard model on a square-lattice

The data sets for $U_{c1}(T)$ and $U_{c2}(T)$ were calculated for the same temperatures and similarly fitted with the program *gnuplot*. Due to the relatively small variation w.r.t. U, it is not a priori obvious which function yields the best fit for $U_{c1}(T)$.
Several functions used to fit $U_{c1}(T)$ are shown in Fig. 24, and listed in the following.

- $g_1(x) = a_1 + b_1 x$
- $g_2(x) = a_2 + b_2 x^{c_2}$
- $g_3(x) = a_3 + b_3 e^{c_3 x}$
- $g_4(x) = 0.043 - \frac{1}{a_4(x-2.3)}$
- $g_5(x) = 0.043 - \frac{1}{a_5(x-2.3)^{b_5}}$

- $g_6(x) = 0.9 - \frac{1}{a_6(x-2.3)^{b_6}}$
- $g_7(x) = 0.9 - \frac{1}{a_7(x-b_7)^{c_7}}$

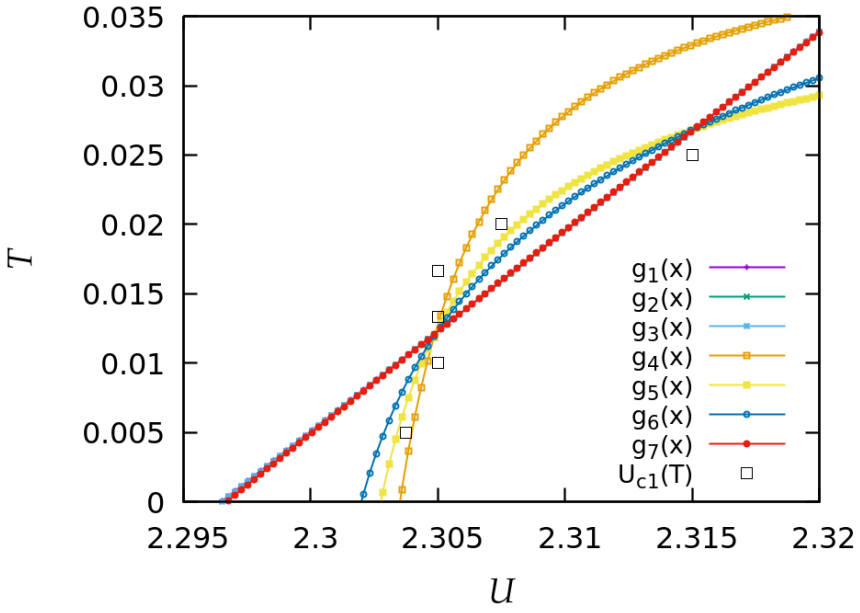

Figure 24: $U_{c1}(T)$ of the square-lattice fitted by different functions.

The function g_1 is a linear fit. The fits g_2 and also g_3 are similar to the linear solution of g_1. Polynomials with order greater than one yield a non-physical solution, because the slope of the functions changes the sign and thus these functions are not shown in Fig. 24. The functions g_4, g_5, g_6 and g_7 are constructed to get a closer fit. This works for the functions g_4, g_5 and g_6. But for g_7, which has a additional fitting parameter, the solution is similar to the linear fit of g_1. The function which yields the best solution is not distinct. The choice of the function, which has been used for DMFT phase-diagram, is the linear fit because it is the solution of three different fits. The Functions shown Fig. 23:

- $h_1(x) = a_1 + b_1 x^{c_1} \quad for \quad U_{c1}$
- $h_2(x) = a_2 + b_2 e^{c_2 x} \quad for \quad U_{c2}$

Fig. 23 shows that with decreasing temperature, $U_{c1}(T)$ decreases (contrary to the Bethe case) while $U_{c2}(T)$ increases. The corresponding critical end-point and the phases of the Hubbard model on a square lattice are shown in the same way as in Fig. 22.

3 Comparison and Discussion

The Bethe-lattice and the square-lattice DMFT phase-diagrams are shown in a single figure (Fig. 25) for comparison.

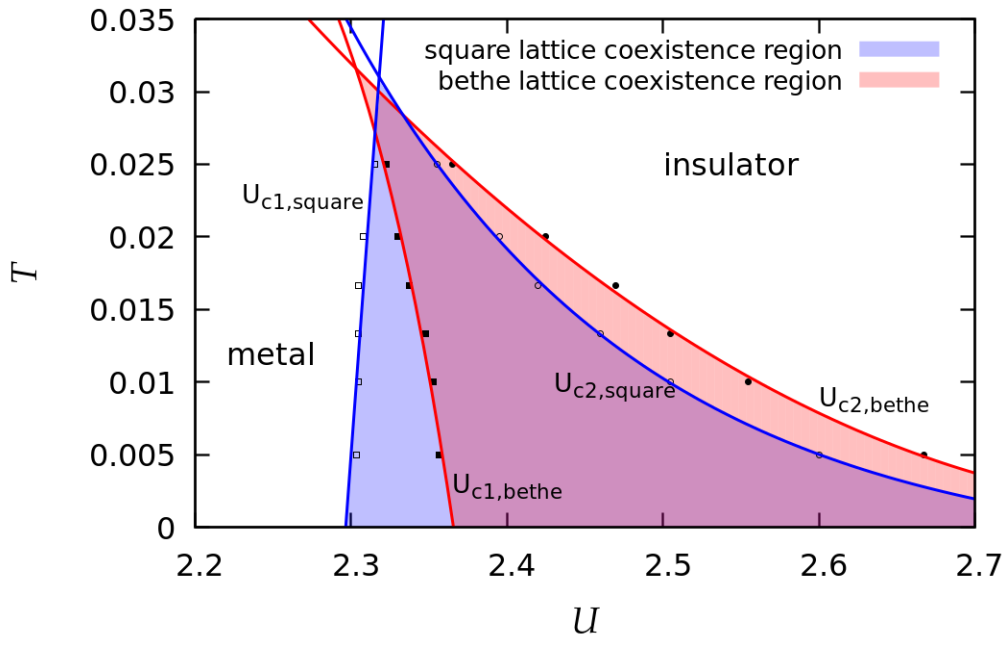

Figure 25: Comparison of the DMFT coexistence region of the Hubbard model on a Bethe-lattice and on a square-lattice, respectively. The red area corresponds to the Bethe-lattice and the blue one to the square-lattice.

At first Fig. 25 shows that for all calculated temperatures the critical interactions $U_{c1}(T)$ and $U_{c2}(T)$ of the square-lattice have lower values U than the ones of the Bethe-lattice. Thus the square-lattice coexistence region (blue area) is slightly shifted leftwards to the Bethe-lattice one (red area). Secondly, Fig. 25 shows that the width of both coexistence regions are nearly equal. The behavior of $U_{c2}(T)$ for both lattices are similar and thus also the fitted functions. A quantitative difference between the phase-diagrams is the behavior of the $U_{c1}(T)$. For the $U_{c1,bethe}(T)$ the critical interaction values increase with decreasing T, below the critical endpoint. On the other side, for $U_{c1,square}(T)$ the critical interaction values decrease. This gives the square-lattice phase-diagram a qualitatively different shape to the Bethe-lattice phase-diagram.

4 Conclusion

In this Bachelor thesis we studied the difference of the MIT in the DMFT solution of the Hubbard model on the Bethe-lattice and the 2D-square-lattice. Starting from the corresponding DOSes, exploiting the *w2dynamics*-package as impurity solver, DMFT calculations have been done.
A typical output of the calculations is the self-energy and the double occupancy, which are used to estimate $U_{c1}(T)$ and $U_{c2}(T)$, separately for both lattices to get a lead whether the differences in the physical MIT can effect the low temperature behavior of the irreducible vertex divergences.

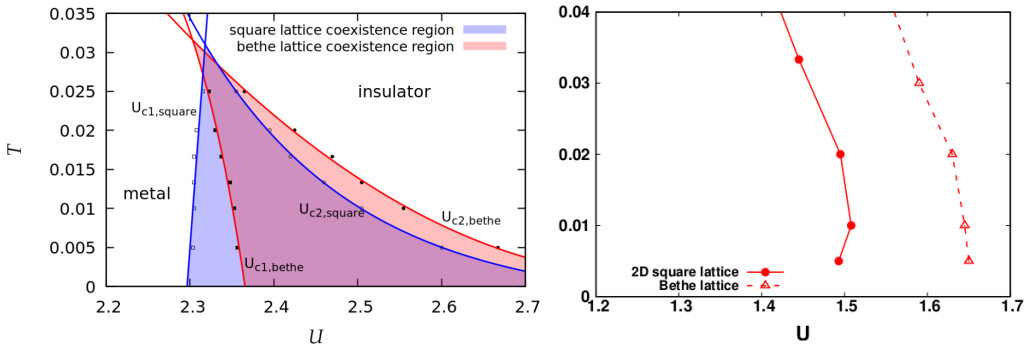

(a) Phase-diagram of the Mott-Hubbard-transition on the Bethe-lattice and the 2D-square-lattice

(b) First divergence line for the 2D square lattice (solid line) and the Bethe lattice (dashed line) at low temperature, taken from [9]

Figure 26: Comparison of the irreducible vertex divergences in the Hubbard model and the Mott-Hubbard transition, of the Bethe-lattice and the 2D-square-lattice

Fig. 26 shows the phase-diagrams and the divergence lines next to each other for a better comparison. This illustrates that for decreasing temperature the divergence lines are getting closer to the shape of $U_{c1}(T)$ lines of the phase-diagram. So the overall slope of divergence lines might indeed be related to the $U_{c1}(T)$ lines of the MIT. To confirm this assumption more studies are necessary, also because the divergence of the irreducible vertexes might else appear in model without a MIT [10].
More over, it would be also interesting to determine, through is a minimization of the free energy whether the first order transition line of MIT is also effected by the lattice details.

References

[1] A. Toschi. "Local electronic correlations". In: *QFT-Lecture TU Wien, LVA 138.062* (2016).

[2] M. P. Marder. *Condensed Matter Physics, 2nd Edition*. 2nd ed. Wiley, 2010. Chap. 17.5.

[3] J. Hubbard. "Electron Correlations in Narrow Energy Bands". In: *Proceedings of the Royal Society of London. Series A, Mathematical and Physical Sciences* 276.1365 (1963), pp. 238–257. URL: www.jstor.org/stable/2414761.

[4] E. Pavarini et al. "The LDA+DMFT approach to strongly correlated materials". In: *Schriften des Forschungszentrums Jülich Reihe Modeling and Simulation* 1 (2011).

[5] M. W. Kinza. "Single Impurity Anderson Model and Dynamical Mean Field Theory". In: *Dissertation - RWTH Aachen* (2003). URL: http://publications.rwth-aachen.de/record/229234/files/4979.pdf.

[6] A. Georges et al. "Dynamical mean-field theory of strongly correlated fermion systems and the limit of infinite dimensions". In: *Rev. Mod. Phys.* 68 (1996), pp. 13–125. DOI: 10.1103/RevModPhys.68.13.

[7] A. Toschi. "Strong Electronic Correlation in Dynamical Mean Field Theory and beyond". In: *Habilitationsschrift TU Wien* (2011).

[8] G. Kotliar and D. Vollhardt. "Strongly Correlated Materials: Insights From Dynamical Mean-Field Theory". In: *Physics Today* 57 (2004), pp. 53–59.

[9] T. Schäfer et al. "Nonperturbative landscape of the Mott-Hubbard transition: Multiple divergence lines around the critical endpoint". In: *Phys. Rev. B.* 94 (2016). DOI: 10.1103/PhysRevB.94.235108. arXiv: 1606.03393.

[10] P. Chalupa et al. "Divergences of the irreducible vertex functions in correlated metallic systems: Insights from the Anderson Impurity Model". In: *ArXiv e-prints* (2017). arXiv: 1712.04171.

[11] N. Blümer. "Mott-Hubbard Metal-Insulator Transition and Optical Conductivity in High Dimensions". In: *Dissertation - Universität Mainz* (2003). URL: http://www.komet337.physik.uni-mainz.de/Dateien/bluemer_color.pdf.

[12] M. Wallerberger. “w2dynamics: Continuous time quantum Monte Carlo calculations of one- and two-particle propagators”. In: *Dissertation - TU Wien* (2016). URL: http://repositum.tuwien.ac.at/obvutwhs/content/titleinfo/1370376.

[13] M. Wallerberger et al. “w2dynamics: Local one- and two-particle quantities from dynamical mean field theory”. In: *ArXiv e-prints* (2018). arXiv: 1801.10209.